

See discussions, stats, and author profiles for this publication at: <https://www.researchgate.net/publication/7367378>

Experimental and Theoretical Differential Cross Sections for the $N(2D) + H_2$ Reaction †

ARTICLE in THE JOURNAL OF PHYSICAL CHEMISTRY A · FEBRUARY 2006

Impact Factor: 2.69 · DOI: 10.1021/jp054928v · Source: PubMed

CITATIONS

71

READS

36

7 AUTHORS, INCLUDING:



Nadia Balucani

Università degli Studi di Perugia

162 PUBLICATIONS 3,468 CITATIONS

SEE PROFILE



Piergiorgio Casavecchia

Università degli Studi di Perugia

168 PUBLICATIONS 4,322 CITATIONS

SEE PROFILE



Tomas Gonzalez-Lezana

Spanish National Research Council

105 PUBLICATIONS 1,540 CITATIONS

SEE PROFILE

Experimental and Theoretical Differential Cross Sections for the $\text{N}(^2\text{D}) + \text{H}_2$ Reaction[†]

Nadia Balucani and Piergiorgio Casavecchia*

Dipartimento di Chimica, Università di Perugia, 06123 Perugia, Italy

Luis Bañares and F. Javier Aoiz

Departamento de Química Física, Facultad de Química, Universidad Complutense, 28040 Madrid, Spain

Tomás Gonzalez-Lezana

Instituto de Matemáticas y Física Fundamental, Consejo Superior de Investigaciones Científicas, Serrano 123, 28006 Madrid, Spain

Pascal Honvault and Jean-Michel Launay

PALMS, UMR 6627 du CNRS, Université de Rennes 1, Campus de Beaulieu, 35042 Rennes Cedex, France

Received: August 31, 2005; In Final Form: October 6, 2005

In this paper, we report a combined experimental and theoretical study on the dynamics of the $\text{N}(^2\text{D}) + \text{H}_2$ *insertion* reaction at a collision energy of 15.9 kJ mol^{-1} . Product angular and velocity distributions have been obtained in crossed beam experiments and simulated by using the results of quantum mechanical (QM) scattering calculations on the accurate *ab initio* potential energy surface (PES) of Pederson et al. (*J. Chem. Phys.* **1999**, *110*, 9091). Since the QM calculations indicate that there is a significant coupling between the product angular and translational energy distributions, such a coupling has been explicitly included in the simulation of the experimental results. The very good agreement between experiment and QM calculations sustains the accuracy of the NH_2 *ab initio* ground state PES. We also take the opportunity to compare the accurate QM differential cross sections with those obtained by two approximate methods, namely, the widely used quasiclassical trajectory calculations and a rigorous statistical method based on the coupled-channel theory.

I. Introduction

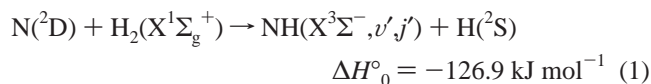
The interaction between experiment and theory has been essential for the progress of the field of reaction dynamics. Indeed, only the direct comparison between detailed experimental observables, such as the differential cross section (DCS), and the results of quantum mechanical (QM) scattering calculations can assess the quality of a computed potential energy surface (PES) and, in turn, allows the knowledge of the factors which underlie a chemical transformation. Until very recently, such an ambitious goal had been achieved only for a few simple direct *abstraction* reactions (such as $\text{H} + \text{H}_2$, $\text{F} + \text{H}_2$, and $\text{Cl} + \text{H}_2$).^{1–9} In the past few years, following the development of an efficient body-frame hyperspherical coordinate method developed by two of the present authors, the same combined experimental and theoretical approach has also been applied to the more complex family of *insertion* reactions, which occur on PESs characterized by deep wells associated to bound intermediates. The method has been successfully applied to study simple *insertion* reactions^{10–13} for which accurate PESs^{14–21} and experimental DCSs are available,^{22–36} namely, $\text{N}(^2\text{D}) + \text{H}_2$, $\text{O}(^1\text{D}) + \text{H}_2$, $\text{C}(^1\text{D}) + \text{H}_2$, and $\text{S}(^1\text{D}) + \text{H}_2$. In all cases, the QM predictions compare well with the experimental results, thus confirming the substantial accuracy of the computed PESs.^{37–41}

Nevertheless, the body-frame hyperspherical coordinate calculations are very computer-time-consuming, even for the simplest *insertion* reactions mentioned above, and alternative approaches are still necessary. That motivates the use of other methods, such as the quasiclassical trajectory (QCT)^{14–16,20–23,26,29–32,34} or time-dependent calculations.^{2,4,42} More recently, a rigorous statistical method (SM) based on the coupled-channel theory was developed,⁴³ which, by making use of the additional random-phase approximation, can generate DCSs for simple insertion reactions.⁴⁴ A similar idea has been exploited also in a wave packet based statistical model.⁴⁵

The accuracy of the alternative approaches should be tested via a comparison with the QM predictions, when available, performed on the same PESs. Interestingly, such a comparison with the QCT calculations has pointed out that the QCT method might be accurate enough when using a Gaussian-weighted binning procedure rather than the usual histogramatic method.^{12,41} Also, the SM results were found to be in excellent agreement with the QM results for the two reactions $\text{C}(^1\text{D}) + \text{H}_2$ and $\text{S}(^1\text{D}) + \text{H}_2$.⁴⁴ However, because the QM DCSs for the reactions with $\text{N}(^2\text{D})$ and $\text{O}(^1\text{D})$ exhibit a slight forward/backward asymmetry, the agreement with the SM for these reactions is not quite so good.⁴⁴

Different from the other simple *insertion* reactions, which are all barrier-less and almost gas-kinetic, the title reaction

[†] Part of the special issue "Donald G. Truhlar Festschrift".



is characterized by an activation energy of 7.1 kJ mol^{-1} , as derived from rate constant measurements in the temperature range 213–300 K.^{46,47} The rate constant at 300 K has been determined to be $2.44(\pm 0.34) \times 10^{-12} \text{ cm}^3 \text{ s}^{-1}$.⁴⁶ The presence of collinear and C_{2v} barriers characterizes the NH_2 ab initio PES derived by Pederson et al.¹⁴ The calculated saddle point energy for the favorite perpendicular approach was found to be 7.9 kJ mol^{-1} . On the same PES, the intermediate well energy was found to be $-525.0 \text{ kJ mol}^{-1}$, which compares well with the experimental value $-520.9 \text{ kJ mol}^{-1}$.¹⁴ Interestingly, in the case of the title reaction, some quantum effects have been noted from the comparison between QM and QCT DCSs³⁷ and, while the QM calculations on the PES of Pederson et al. predict a value of the rate constant at 300 K of $2.51 \times 10^{-12} \text{ cm}^3 \text{ s}^{-1}$, the QCT value is lower than the experimental one, being $1.90 \times 10^{-12} \text{ cm}^3 \text{ s}^{-1}$.³⁷

In a previous account, some of the present authors already reported on the status of the comparison between QM and QCT calculations carried out on the PES by Pederson et al.¹⁴ and the experimental DCSs, as derived from a crossed beam experiment with mass-spectrometric detection.³⁷ The focus of that letter was essentially on the observation of quantum effects manifested from the direct comparison between QM and QCT DCSs for the title reaction. The present paper is a full account of that work, with some important differences. On one hand, a thorough report of the experimental results is given and the experimental center-of-mass best-fit functions are shown. On the other hand, since it has been recognized that for reactions such as $\text{N}(^2\text{D}) + \text{H}_2$ there is a significant coupling between the product angular and translational energy distributions^{28–30,34,35,38,40} and that such a coupling could affect the simulation of the experimental results,^{33,34,40} the QM and QCT DCSs have been used in the simulation program by explicitly considering that coupling. Finally, the efficiency of the SM method for the title reaction is tested with a direct comparison, for the first time, with experimental, QM, and QCT results. As already done before, to remove any possible ambiguity associated with the derivation of the best-fit center-of-mass (CM) functions from the laboratory (LAB) data, the comparison between theoretical and experimental results will be performed by directly simulating the experimental distributions in the LAB frame.

The paper is organized as follows. In section II, the experimental method is briefly described and the experimental results and data analysis are reported. In section III, details of the QM, SM, and QCT methods and calculations are given. Experimental results and theoretical predictions are compared in section IV. The Discussion and Conclusions are presented in section V.

II. Experimental Results and Analysis

A. Crossed Molecular Beam Experiments. The scattering experiments were carried out by using a crossed molecular beam apparatus that has been described in detail elsewhere.⁴⁸ Briefly, two well collimated supersonic beams of the reagents are crossed at 90° in a large scattering chamber with background pressure in the 10^{-7} mbar range, which ensures single collision conditions. The detection system consists of a tunable electron impact ionizer, a quadrupole mass filter, and an off-axis (90°) secondary electron multiplier. The ionizer is located in the innermost region

of a triply differentially pumped ultrahigh-vacuum chamber which is maintained in the 10^{-11} mbar pressure range in operating conditions. The whole detector unit can be rotated in the collision plane around an axis passing through the collision center. Product and reagent velocities are derived from time-of-flight (TOF) measurements.

The study of reaction 1 has been possible following the development in our laboratory of a continuous supersonic beam of nitrogen atoms containing, in addition to the electronic ground state ^4S , a sizable amount of the excited metastable state ^2D . The atomic nitrogen beam is generated by the high-pressure radio frequency discharge beam source successfully used in our laboratory over a number of years to generate intense supersonic beams of atoms and radicals.⁴⁹ The beam was skimmed by a boron nitride skimmer (diameter 1.0 mm) located at a distance of 5.2 mm from the nozzle and further collimated by a rectangular slit. Starting from dilute mixtures of N_2 (2.5%) in He, a high degree of molecular dissociation ($\sim 60\%$) was achieved. Atomic nitrogen was produced in a distribution of electronic states which has been characterized by Stern–Gerlach magnetic analysis:⁴⁹ 72% of the N atoms were found in the ground ^4S state, and 21 and 7%, in the metastable excited ^2D and ^2P states (lying 230.5 and 343.5 kJ mol^{-1} , respectively, above the ground state).⁵⁰ The use of nitrogen atom beams, which contain, in addition to $\text{N}(^2\text{D})$, also $\text{N}(^4\text{S})$ and $\text{N}(^2\text{P})$, does not represent a complication in the present studies, since the reaction of $\text{N}(^4\text{S})$ with H_2 is strongly endoergic ($\Delta H^\circ_0 = 103.6 \text{ kJ mol}^{-1}$)⁴⁷ and that of $\text{N}(^2\text{P})$ is about 2 orders of magnitude slower ($k_{298\text{K}} = 1.4 \times 10^{-14} \text{ cm}^3 \text{ s}^{-1}$) than that of $\text{N}(^2\text{D})$.⁴⁶ In addition, the extent of the product translational energy, E'_T , release fully confirms that the measured NH product is all coming from the reaction with $\text{N}(^2\text{D})$ atoms. In the present experiment, the atomic nitrogen beam was obtained by discharging 250 mbar of the N_2/He mixture at 300 W; a peak velocity of 2860 m s^{-1} and a speed ratio of 6.0 were obtained. The angular divergence was 2.3° .

The beam of H_2 was produced by supersonic expansion through a $70 \mu\text{m}$ stainless steel nozzle of $n\text{-H}_2$, at a stagnation pressure of 2.0 bar with the nozzle resistively heated at 440 K. The peak velocity and speed ratio were 3160 m s^{-1} and 12.0, respectively. The beam angular divergence was about 5° .

Under the present experimental conditions, the collision energy, E_c , was 15.9 kJ mol^{-1} .

Since the calculated DCSs for reaction 1 have been found to be slightly different for different initial rotational states of H_2 ,³⁷ it is certainly important to know the relative rotational state populations of the $n\text{-H}_2(j)$ in the beam. We have not directly characterized the rotational distribution of H_2 in our beam; however, we can refer to the experimental determinations of Pollard et al.⁵¹ because of the strong similarities of expansion conditions (in particular, same nozzle diameter and very similar temperature and stagnation pressure). We have verified that the characterization of the H_2 rotational distribution by Pollard et al. is in agreement with our experimental conditions. We have derived, in fact, the H_2 rotational energy by difference with respect to the amount of the H_2 beam translational energy (as it was determined by the TOF technique),⁵² after calibrating the thermocouple which reads the nozzle temperature in a pure He expansion. Since the value was consistent, the rotational populations we have used in the simulations of our experiment are the following: $P(j=0) = 0.142$, $P(j=1) = 0.590$, $P(j=2) = 0.123$, and $P(j=3) = 0.128$. We recall that the rotational energies of the $j = 1, 2$, and 3 levels of H_2 are 1.42, 4.23, and 8.49 kJ mol^{-1} ,⁵³ respectively.

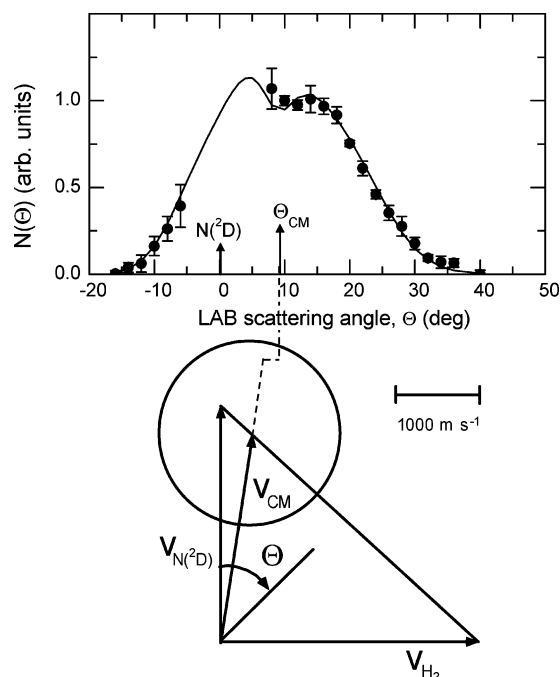


Figure 1. NH product laboratory angular distribution from the reaction $\text{N}(\text{D}) + \text{H}_2$ at $E_c = 15.9 \text{ kJ mol}^{-1}$ and the corresponding canonical Newton diagram. $\mathbf{v}_{\text{N}(\text{D})}$ and \mathbf{v}_{H_2} are the laboratory beam velocity vectors, and Θ_{CM} indicates the location of the CM angle in the LAB frame. The circles in the Newton diagram delimit the maximum speed that NH can attain if all of the available energy is channelled into product translation. The solid line represents the best-fit angular distribution as obtained from the best-fit CM angular and translational energy distributions of Figure 3.

The LAB angular distributions of the NH product, $N(\Theta)$, were obtained by taking several scans of 30 s counts at each scattering angle. The nominal angular resolution of the detector for a point collision zone is 1° . The secondary target beam (H_2 beam) was modulated at 160 Hz by a tuning fork chopper. The background and signal plus background counts are obtained from a pulse counting dual scaler, synchronously gated with the tuning fork.

Product velocity distributions were obtained at selected laboratory angles using the cross-correlation TOF technique: a pseudorandom chopper (145 mm diameter, 0.1 mm thick) with four 127-bit pseudorandom sequences was spun at 393.7 Hz corresponding to a dwell time of $5 \mu\text{s/channel}$. The flight length was 24.6 cm. Counting times varied from 30 to 60 min depending on the signal intensity.

B. Results and Analysis. The LAB product angular distribution at $E_c = 15.9 \text{ kJ mol}^{-1}$ is shown in Figure 1 together with the relative canonical Newton diagram. Because of the presence of the ^{15}N isotope (the natural isotopic abundance is 0.37%), the data, collected at a mass-to-charge ratio (m/e) of 15 (corresponding to NH^+), had to be corrected for the contribution of the elastically scattered ^{15}N . Both ^{14}N and ^{15}N are produced in the beam source from dissociation of molecular nitrogen, with the same velocity and beam characteristics. We have, therefore, performed accurate measurements of the laboratory distributions at $m/e = 15$, due to both reactive scattering signal and elastic scattering of the isotope ^{15}N , and at $m/e = 14$, so that, by using the appropriate density ratio $n(^{15}\text{N})/n(^{14}\text{N})$, we have been able to evaluate and subtract the elastic contribution from the elastic + reactive distribution. In fact, because of the very little difference in mass, the elastic scattering properties of the two isotopes are about the same and the two LAB elastic distributions can be assumed identical. We also verified this assumption by measuring the elastic scattering distributions of both nitrogen

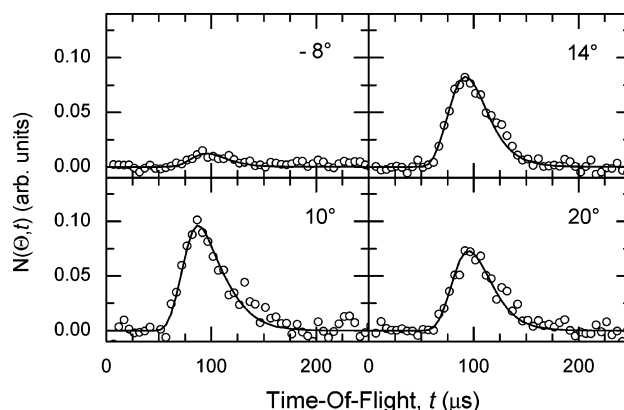


Figure 2. Time-of-flight spectra at $E_c = 15.9 \text{ kJ mol}^{-1}$ for selected LAB angles. The solid lines represent the best-fit distributions calculated when using the best-fit CM functions of Figure 3.

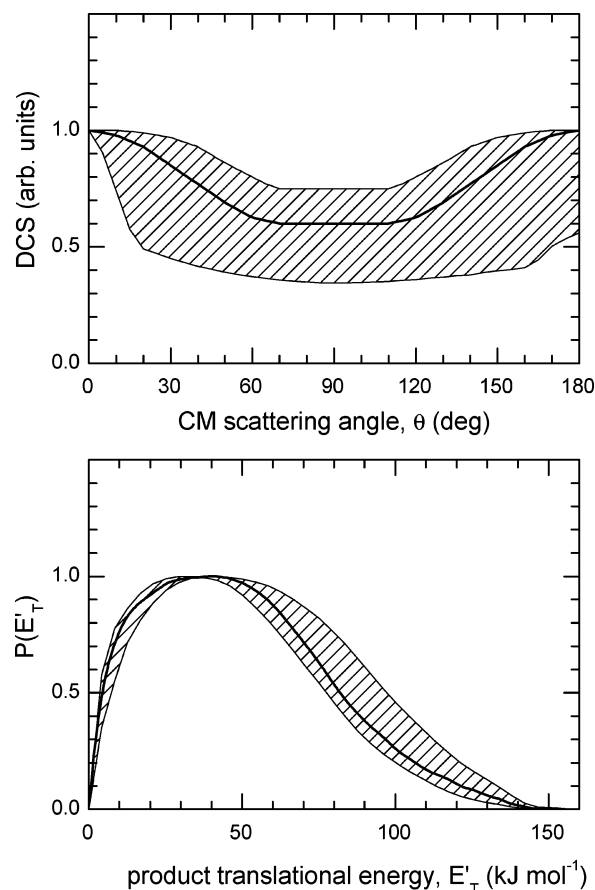


Figure 3. Best-fit CM product (top) angular and (bottom) translational energy distributions at $E_c = 15.9 \text{ kJ mol}^{-1}$. The shaded areas delimit the range of functions which still afford a good fit of the experimental data.

isotopes from He. The same kind of subtraction has been done for the TOF spectra shown in Figure 2. The error bars in Figure 1 indicate plus/minus one standard deviation and include the uncertainty originating from the subtraction of the elastic contribution. The solid lines represent the curves calculated by using the best-fit CM functions of Figure 3 (see below).

As is well visible from Figure 1, the measured angular distribution extends on both sides of the CM angle, Θ_{CM} , which is the expected result for a reaction which proceeds via a long-lived complex or which involves a symmetric intermediate, such as NH_2 . The angular distribution is relatively broad and fits within the limit of energy conservation, as indicated by the circle

in the Newton diagram which has been drawn assuming that all of the available energy is released as product translational energy.

For the physical interpretation of the scattering results, the angular and TOF distributions measured in the LAB velocity frame are transformed to the CM frame. Because of the finite resolution of experimental conditions, analysis of the LAB data is carried out, as usual, by forward convoluting trial CM distributions over the experimental conditions. Since a good fit of the LAB distributions could be achieved by using a separable form for the CM product flux distribution [that is, the CM flux could be conveniently represented by $I_{\text{CM}}(\theta, E'_T) = T(\theta) \times P(E'_T)$, where the $T(\theta)$ function represents the CM total DCS and $P(E'_T)$ is the product translational energy distribution], no further attempts at considering the DCS and $P(E'_T)$ coupling were made in the best-fit procedure. Regarding this, the present experimental results are quite different with respect to those of the similar reaction $\text{C}(^1\text{D}) + \text{H}_2$ investigated with the same experimental technique.³³ In that case, a best fit of the experimental results at $E_c = 7.8 \text{ kJ mol}^{-1}$ could only be achieved considering that a larger fraction of energy is released as product translational energy for the products scattered at $\theta = 0\text{--}15^\circ$ and $\theta = 165\text{--}180^\circ$.³³

The energy dependence of the integral cross sections (ICSs), as derived by the QM calculations, has been included in the data analysis; the effect was negligible, however, because of the narrow spread of relative translational energies in these experiments. The best-fit CM angular and translational energy distributions are depicted in Figure 3; the hatched areas delimit the range of CM functions which still afford an acceptable fit to the data; that is, they represent the error bars of the present determination.

The best-fit angular distribution is backward/forward symmetric, even though an angular distribution with a slight preference for forward scattering still gives an acceptable fit of the experimental data, as witnessed by the error bars (hatched area). Also, the degree of polarization (with polarization of the CM angular distribution, we mean the ratio in magnitude of sideways scattering as compared to the forward and backward scattering), which for the best-fit CM function is $T(90^\circ)/T(0^\circ) = 0.60$, may vary from 0.75 to 0.35. The relatively broad error bars associated with the experimental differential cross section are due to the unfavorable kinematics of this experiment. The peak in the forward direction is, in fact, partially missed because of the "blind" angular range close to $\Theta = 0^\circ$ where the detector cannot be placed. Interestingly, the best-fit $T(\theta)$ function is practically identical to the one derived for the experiment on $\text{N}(^2\text{D}) + \text{D}_2$ at the same E_c value (and that experiment was characterized by more favorable kinematics), thus implying that there is not a significant isotopic effect.

The average product translational energy, $\langle E'_T \rangle$, is 49.7 kJ mol^{-1} , that is, about 35% of the total available energy (the total available energy is given by the sum of the collision energy and of the reaction exothermicity⁴⁷). This modest fraction of energy released as translational motion of the products points to a high internal (rovibrational) excitation, as seen in spectroscopic studies.

We wish to stress that the fit of the experimental data was extremely sensitive to the rise of $P(E'_T)$ in the $E'_T = 0\text{--}5 \text{ kJ mol}^{-1}$ range, while it was less responsive to the details of the $P(E'_T)$ tail. This is well represented by the shape of the hatched area that delimits the range of $P(E'_T)$ functions generating an acceptable fit of the experimental data.

III. Theoretical Methods and Results

A. Quantum Mechanical Calculations. The QM scattering calculations have been performed using a time-independent method based on body-frame democratic hyperspherical coordinates⁵⁴ on the ab initio PES of Pederson et al.,¹⁴ at the collision energy of the experiment and for H_2 rotational states $j = 0\text{--}2$. To correctly simulate the LAB distributions, the DCS for initial $j = 3$ is also necessary, as the population of the $j = 3$ level in the H_2 beam is not negligible. However, the QM calculations for initial $j = 3$ require a very large computer time. At the lower E_c value 8.8 kJ mol^{-1} , where the scattering calculations are much less expensive because of the reduced basis set, the DCS of initial $j = 3$ was found to be very similar to that of $j = 2$. Therefore, to simulate the experimental results (see below), we have assumed that the DCS for initial $j = 2$ and 3 are the same also at 15.9 kJ mol^{-1} .

At a set of 30 hyperradii, ρ_p , we have built a set of surface states which are eigenfunctions of a fixed-hyperradius reference Hamiltonian, $H_0 = T + V$, which incorporates the kinetic energy, T , arising from deformation and rotation around the body-frame axis of least inertia Z and the potential energy V . At a small hyperradius, the surface states span a large fraction of configuration space and allow for atom exchange. They are also eigenfunctions of the projection J_Z of the total angular momentum on the axis of least inertia with quantum number Ω and are computed by a variational expansion on a basis of pseudo-hyperspherical harmonics⁵⁴ with a maximum grand-angular momentum equal to 218 for the even parity states and equal to 219 for the odd parity states. The number of pseudo-hyperspherical harmonics varies between 3080 for $\Omega = 0$ and 1806 for $\Omega = 26$.

The total wave function is expanded on the surface states in small sectors around each ρ_p . The coefficients of the expansion satisfy a set of second-order coupled differential equations with couplings arising from the difference between the exact Hamiltonian and the reference Hamiltonian. Propagation of the total wave function goes from $\rho = 1.8a_0$ up to the asymptotic matching distance at $7.8a_0$, where the S matrix is extracted with a total number of 30 sectors of equal size. The crucial parameters for convergence are essentially the number of surface states to be included. For total angular momentum $J = 0$, the scattering wave function is expanded on the basis of 217 surface states for even permutation symmetry and 215 for odd permutation symmetry. These states dissociate at large hyperradius into the NH (35,32,30,27,24,20,16,11) rovibrational set (this notation indicates the largest rotational level j for each vibrational manifold $v = 0, 1, \dots, 7$) and the H_2 (12,8,2) set for even H–H permutation symmetry (even j 's) and the H_2 (11,7,3) set for odd permutation symmetry (odd j 's). Convergence of reaction probabilities was asserted by comparison with calculations performed with several bases including up to 290 states. When computing $J \neq 0$ partial waves, we had to include all possible Ω components in the close-coupling expansion, to obtain accurate integral and differential cross sections. Thus, $\Omega_{\text{max}} = J$, and the number of coupled equations increases from 217 for $J = 0$ to 2917 for $J = 26$ and even permutation symmetry and from 215 for $J = 0$ to 2905 for $J = 26$ and odd permutation symmetry.

B. Statistical Calculations. A statistical quantum study of the title reaction has been performed by means of the SM described in ref 44. In this approach, the existence of deep potential wells in the PESs of insertion reactions is supposed to guarantee the formation of an intermediate complex in the path between reactants and products. A long enough lifetime

for such a collision complex enables a statistical treatment of its formation and decay as independent events. Within the SM framework, the state-to-state probability describing the reactive process between an initial (v, j, k) state at the reactant channel α and a final (v', j', k') state at the product channel α' at total energy E and total angular momentum J and parity I is approximated as

$$|S_{\alpha'v'j'k',\alpha vjk}^{JJ\alpha'}(E)|^2 \cong \frac{p_{v'j'k'}^{JJ\alpha'}(E) p_{vjk}^{JJ\alpha}(E)}{\sum_{\alpha''v''j''k''} p_{v''j''k''}^{JJ\alpha''}(E)} \quad (2)$$

where the sum in the denominator runs for all energetically accessible diatom states. The quantities $p_{vjk}^{JJ\alpha}(E)$ and $p_{v'j'k'}^{JJ\alpha'}(E)$ are capture probabilities, which may be interpreted as the probability of formation of the intermediate complex from the initial (v, j, k)-state and the probability of decay of the intermediate complex to the final (v', j', k') state, and are calculated separately for each arrangement α as

$$p_{vjk}^{JJ\alpha}(E) = 1 - \sum_{v'j'k'} |S_{v'j'k',vjk}^{JJ\alpha}(E)|^2 \quad (3)$$

The open-channel scattering matrix in eq 3 is obtained by solving a usual set of close-coupled equations within the centrifugal-sudden (CS) approximation.⁴⁴ The use of the CS approximation in this case does not produce significant effects on the ICSs and DCSs when compared with those obtained by the accurate coupled-channel treatment as shown elsewhere.^{43,44}

Whereas the ICS can be evaluated from the exact QM expression by simply introducing the corresponding statistical approximation of eq 2, the calculation of the DCS requires a further approximation. Invoking a random-phase approximation that neglects the interference terms between different values of I and J , the statistical expression of the DCS in the helicity representation is given by⁴⁴

$$\sigma_{\alpha'v'j',\alpha vj}(\theta, E) \cong \frac{1}{8k_{\alpha vj}^2(2j+1)} \sum_{Jk} (2J+1)^2 [|d_{k'k}^J(\pi - \theta)|^2 + |d_{k'k}^J(\theta)|^2] |S_{\alpha'v'j'k',\alpha vjk}^{JJ\alpha'}(E)|^2 \quad (4)$$

where $k_{\alpha vj}^2 = 2\mu(E - E_{vj})/\hbar^2$. μ is the atom–diatom reduced mass, θ is the CM scattering angle, and $d_{k'k}^J(\theta)$ is a reduced rotation matrix element.⁵⁵

The values of the capture radii, R_C , which define in each arrangement the assumed extent of the collision complex, used in the propagation to obtain the scattering matrix (see ref 44 for details) were set up at 1.6 Å for the N + H₂ arrangement and 1.8 Å for the NH + H arrangement in mass scaled coordinates, respectively. The SM calculations have been carried out at $E_c = 15.9$ kJ mol⁻¹ and for H₂ rotational states $j = 0-3$ on the PES by Pederson et al.¹⁴

C. Quasiclassical Trajectory Calculations. The QCT calculations have been performed on the same PES of Pederson et al.¹⁴ by running batches of 10⁵ trajectories at $E_c = 15.9$ kJ mol⁻¹ and for H₂ in the rotational levels $j = 0-3$ following the procedures described elsewhere.⁵⁶ The trajectories were started at a N–H₂ distance of 8 Å, and the integration step size in the trajectories was chosen to be 0.05 fs. This guarantees a total energy conservation better than one part in 10⁴ and conservation of total angular momentum better than one part in 10⁶. The rovibrational energies of the H₂ reagent and those of the NH product were calculated by semiclassical quantization of the

TABLE 1: QM, QCT, and SM Vibrational-State-Resolved ICSs (in Å²) for the Reaction N(²D) + H₂($v=0, j=0-3$) → NH(v') + H at $E_c = 15.9$ kJ mol⁻¹

		total	$v' = 0$	$v' = 1$	$v' = 2$	$v' = 3$	$v' = 4$
QM	$j = 0$	6.68	2.48	1.91	1.40	0.79	0.10
	$j = 1$	6.69	2.41	1.83	1.43	0.86	0.15
	$j = 2$	6.71	2.22	1.83	1.48	0.98	0.20
QCT	$j = 0$	5.81	2.23	1.80	1.23	0.51	0.04
	$j = 1$	5.99	2.22	1.89	1.21	0.63	0.04
	$j = 2$	6.24	2.21	1.86	1.33	0.74	0.10
SM	$j = 3$	6.85	2.20	1.86	1.40	1.26	0.13
	$j = 0$	6.88	2.34	1.95	1.50	0.92	0.16
	$j = 1$	6.85	2.31	1.93	1.49	0.92	0.19
	$j = 2$	6.79	2.24	1.88	1.46	0.94	0.26
	$j = 3$	7.01	2.24	1.90	1.50	1.00	0.36

action using the potential given by the asymptotic diatom limits of the PES. These rovibrational energies were fitted to Dunham expansions containing 20 terms (fourth power in $v + 1/2$ and third power in $j(j + 1)$). The assignment of product quantum numbers v', j' is carried out by equating the classical rotational angular momentum of the product molecule to $[j'(j' + 1)]^{1/2}\hbar$. With the (real) j' value so obtained, the vibrational quantum number v' is found by equating the internal energy of the outgoing molecule to the corresponding Dunham expansion. In the most common procedure, these real v' and j' values are rounded to the nearest integer, in what is named the histogrammatic binning method. In the present work, we have implemented an alternative binning procedure in which a Gaussian function centered at the quantal action and with a given width is employed to weight the trajectories following the criteria that the closer the vibrational action of a given trajectory to the nearest integer, the larger the weighting coefficient for that trajectory. In particular, we have used a full width at half-maximum (fwhm) for the Gaussian functions of 0.1. This Gaussian-weighted binning method is based on an original idea by Bonnet and Rayez,⁵⁷ and it has shown to be very powerful in reproducing correctly QM rotational distributions and reaction thresholds in several insertion reactions.^{12,34,40,41} In the present case, given the large exothermicity of the title reaction, the rotational distributions corresponding to the reaction channels yielding NH molecules with the largest v' values ($v' = 3, 4$), which are the least exoergic, are the most affected by the binning procedure.

DCSs were calculated for every rovibrational state of NH by the method of moments expansion in Legendre polynomials. The Smirnov–Kolmogorov test was used to decide when to truncate the series. Significance levels higher than 99% could be achieved by using 8–16 moments, depending on the number of reactive trajectories available, ensuring good convergence, such that the inclusion of more terms did not produce any significant change.

D. Integral and Differential Cross Sections. The total and v' -state-resolved ICSs for the N(²D) + H₂($v=0, j=0-3$) reactions calculated by means of the QM, SM, and QCT methods at $E_c = 15.9$ kJ mol⁻¹ are listed in Table 1. In general, the QCT total ICSs are somewhat smaller than those obtained in the QM calculations, whereas the SM ICSs are somewhat larger. The most interesting discrepancy between the QCT and the QM and SM results is the different effect of the H₂ rotational excitation on reactivity. In the QCT calculations, rotational excitation always has a beneficial effect, with the total ICS increasing as j increases. However, in the QM case, the total ICS is practically constant and, in the SM calculations, a slight decrease of the total ICS is observed when going from $j = 0$ to $j = 2$. The differences between the QCT and QM total ICSs decrease with

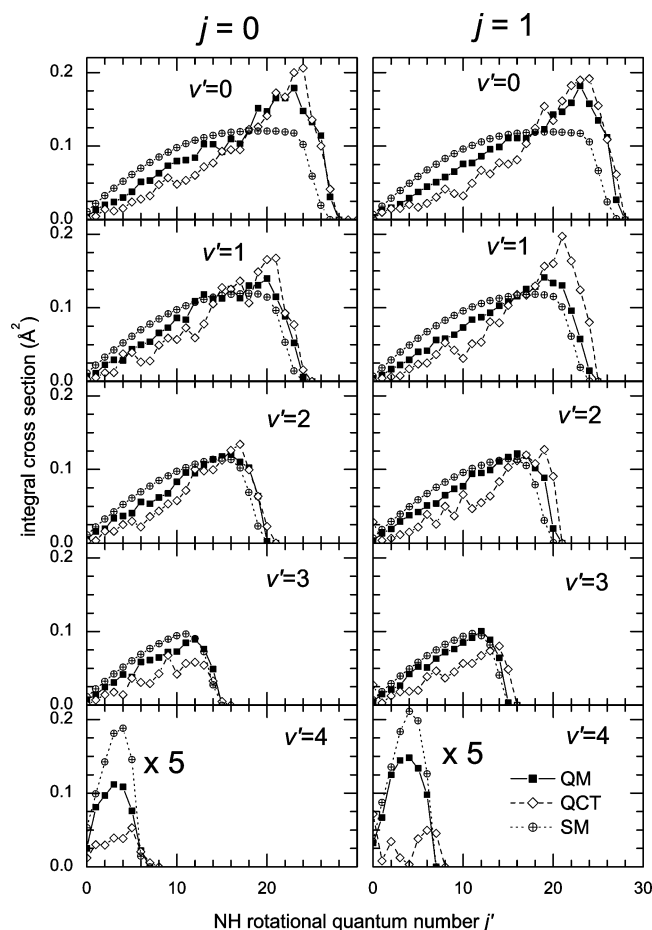


Figure 4. QM, QCT, and SM v' -state-resolved rotational distributions calculated for the $\text{N}(\text{D}) + \text{H}_2(v=0, j=0, 1)$ reaction at $E_c = 15.9 \text{ kJ mol}^{-1}$ on the PES by Pederson et al.¹⁴

increasing j . A possible explanation for such differences, especially for $j = 0$, is the existence of QM effects, such as tunneling, that the QCT method cannot account for.³⁷ In the QM calculations and for low values of j , this tunneling effect might compensate for the beneficial role of reagent rotational excitation, and thus, the net effect of rotational excitation on the overall reactivity is very small. Since the SM treatment is based on the coupled-channel theory, all quantum effects are accurately reproduced and the SM ICSs are in very good accordance with those obtained from the exact QM treatment.^{43,44} Regarding the v' -state-resolved ICSs, although there is good general agreement between the vibrational distributions obtained from the different theoretical calculations, the most important discrepancies between the QCT and QM/SM results are found for $v' > 1$, for which the QCT ICSs are significantly smaller than the QM/SM ones, especially for low j levels. As shown by Umemoto and co-workers (see Figure 3 of ref 58), the QM and QCT vibrational distributions calculated on the PES of Pederson et al. are in excellent agreement with their most recent experimental results and at variance with those of Dodd et al.⁵⁹

The QM, SM, and QCT v' -state-resolved rotational distributions for the title reaction with H_2 in $j = 0$ and $j = 1$ are shown in Figure 4. The corresponding data for $j = 2$ and $j = 3$ are shown in Supporting Information Figure A. The agreement found between QCT and QM rotational distributions is very good, including the largest v' levels of the NH product. For those vibrational states ($v' = 3, 4$) which are the least exoergic, the histogramatic binning procedure in the QCT method yields

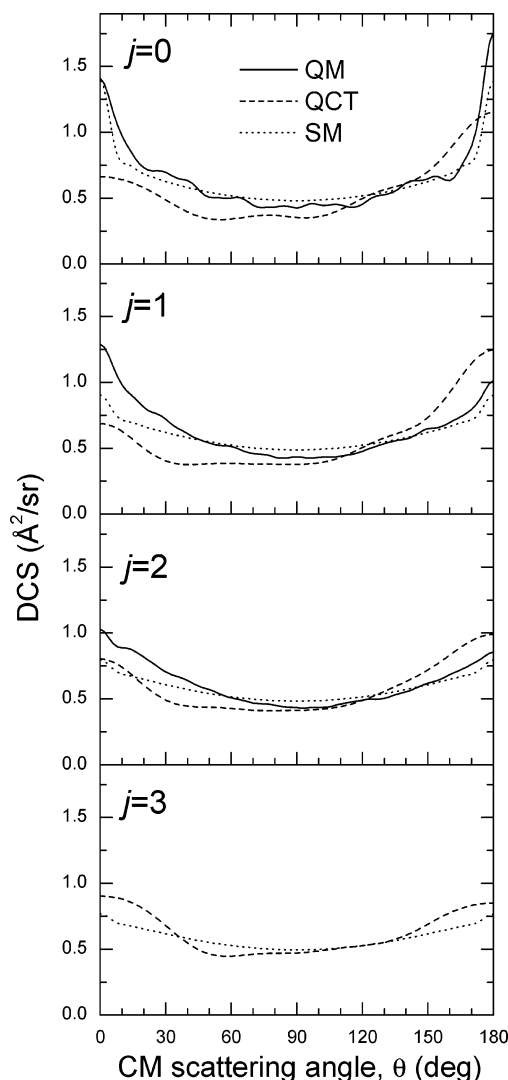


Figure 5. QM, QCT, and SM total differential cross sections calculated for the $\text{N}(\text{D}) + \text{H}_2(v=0, j=0-3)$ reactions at $E_c = 15.9 \text{ kJ mol}^{-1}$ on the PES by Pederson et al.¹⁴ In the QM case, there are no data available for $j = 3$.

rotational distributions hotter than the QM ones (see comments in section III.C and references therein), with the classical distributions reaching j' levels which are energetically forbidden. This problem is fixed when the Gaussian binning procedure is employed. As can be seen, in general, the QCT ICSs underestimate those calculated quantum mechanically for low values of j' , but the shapes of the classical rotational distributions are very similar to those of the QM calculations. In contrast, the SM results always overestimate the QM ICSs for low values of j' and the shapes of the distributions, which are always very similar irrespective of the v' state and initial j value, do not agree so well with the QM ones, especially for $v' = 0$ and $v' = 1$. As v' increases, the agreement between the SM and QM distributions improves. The agreement between the SM and QM rotational distributions was actually seen to be better when not using the CS approximation.⁴³

Figure 5 shows the comparison between the theoretical total DCSs calculated at the different j values. As can be seen, neither the QM nor the QCT DCSs are perfectly backward/forward symmetric for any of the initial j states of H_2 . As already mentioned in ref 37, while the QCT DCSs show a preference for backward scattering, the QM ones show an alternative behavior with the DCS for $j = 0$ favoring backward scattering

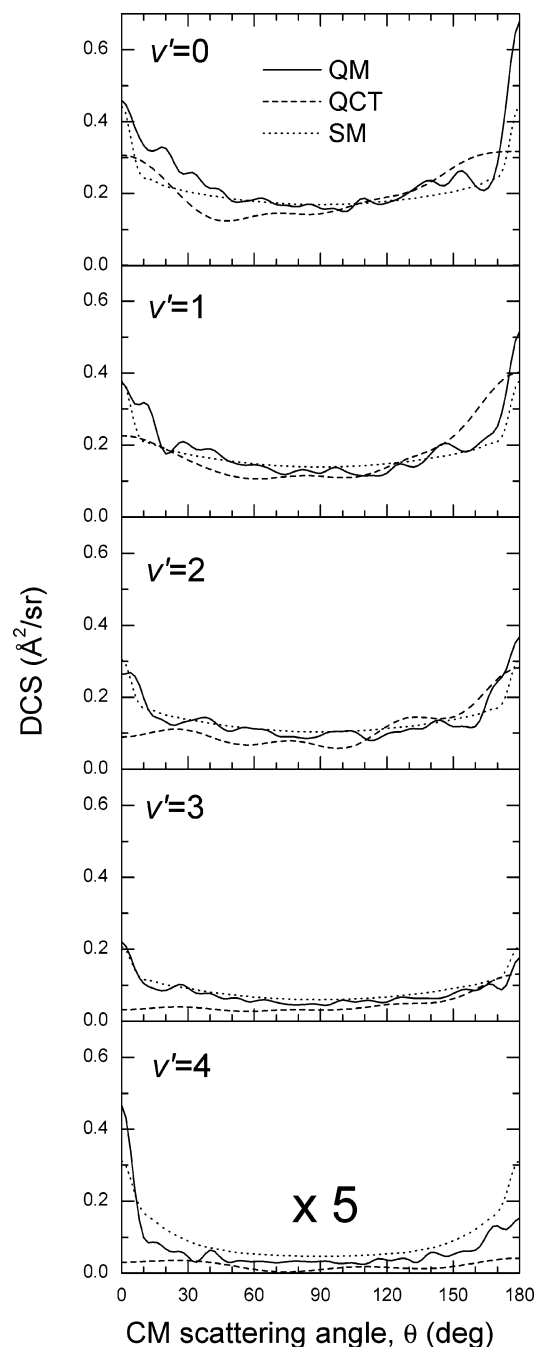


Figure 6. QM, QCT, and SM v' -state-resolved differential cross sections calculated for the $\text{N}(^2\text{D}) + \text{H}_2(v=0, j=0)$ reaction at $E_c = 15.9$ kJ mol^{-1} on the PES by Pederson et al.¹⁴

and those for $j = 1$ and 2 yielding more scattering in the forward direction. For all values of j , there is a clear disagreement between the QCT and QM total DCSs, which is especially important for $j = 0$ and 1. The QCT calculations clearly underestimate the observed QM scattering in the forward hemisphere, and the QCT DCSs are more intense than the QM ones at scattering angles larger than about 120° (backward hemisphere). In addition, for $j = 0$, the QM DCS shows pronounced forward and backward peaks, which are not reproduced by the QCT calculations. As was shown in ref 37 and we will see in section IV of the present work, these discrepancies are very relevant when comparing the theoretical results with the experimental angular distribution. The forward and backward peaks substantially decrease as j increases, and they are qualitatively reproduced by the SM calculations.

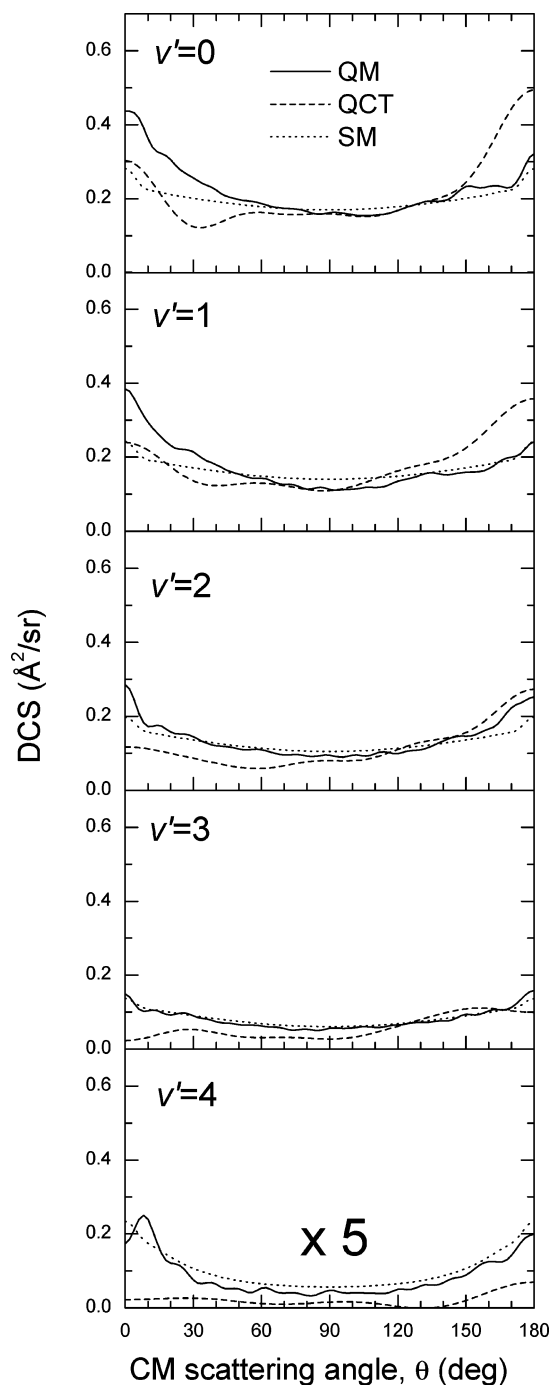


Figure 7. Same as Figure 6 but for the $\text{N}(^2\text{D}) + \text{H}_2(v=0, j=1)$ reaction.

Manolopoulos and co-workers⁴⁴ have observed this behavior in SM calculations for this and other insertion reactions of the family, and it has been attributed to tunneling through the reactant and product centrifugal barrier at the highest total angular momenta contributing to reaction. Clearly, tunneling is not allowed classically, but it is fully integrated in the SM calculations which incorporate the coupled-channels theory. However, it is quite remarkable that the SM calculations cannot totally reproduce the scattering in the forward hemisphere, especially for $j = 1$ and 2, as can be appreciated in Figure 5. In any case, scattering in the forward hemisphere from the SM calculations is larger than that in the QCT DCSs.

The v' -state-resolved DCSs are compared in Figures 6 and 7 for the title reaction with H_2 in $j = 0$ and 1, respectively. The analogous data for $j = 2$ (QM, QCT, and SM) and $j = 3$ (QCT

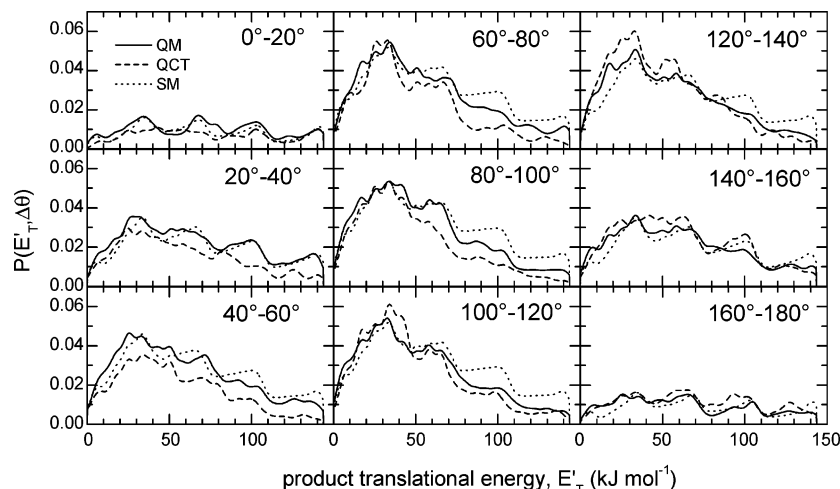


Figure 8. QM, QCT, and SM scattering-angle-selected product translational energy distributions $P(E'_T, \Delta\theta)$ calculated at $E_c = 15.9 \text{ kJ mol}^{-1}$ for H_2 in initial $j = 0$ on the PES by Pederson et al.¹⁴

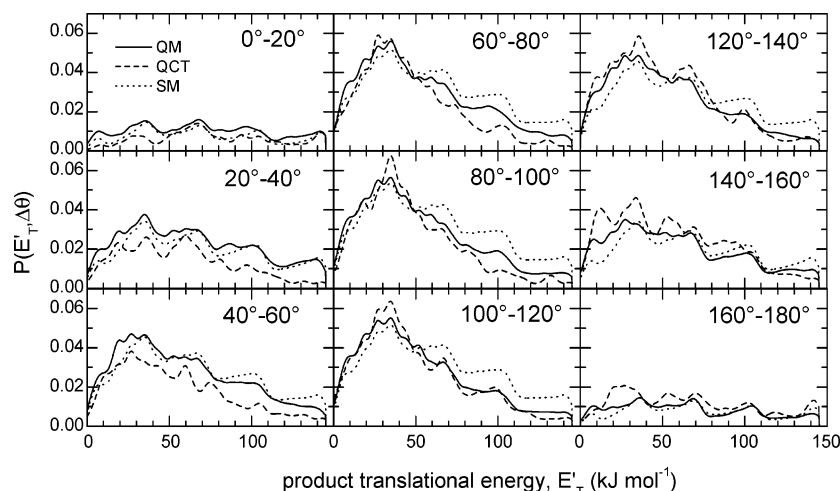


Figure 9. Same as Figure 8 but for the reaction with H_2 in initial $j = 1$.

and SM only) are shown in Supporting Information Figures B and C. As a general trend as for the total DCSs, the same QCT underestimation of forward scattering and overestimation of backward scattering with respect to the QM results is observed for $v' < 3$ levels, which are the NH vibrational levels contributing more to the total ICS. For $v' = 3$ and $v' = 4$, the QCT DCSs are less intense than the QM counterparts in practically the whole scattering angular range. The same discrepancies found for the total DCSs between the SM and QM results are also found in the v' DCSs for $v' = 0$ and $v' = 1$. However, a very good agreement is found for $v' > 1$ in this case. The extreme forward and backward peaks appearing most prominently in the QM v' -state-resolved DCSs for $j = 0$ are qualitatively reproduced by the SM calculations. We note that there is no difference in the total reactivity of $j = 0$ and $j = 1$ in the case of this system (see Table 1), somewhat in contrast with the $\text{O}(\text{1D}) + \text{H}_2$ reaction.²⁴ The effect of rotation on the extreme backward/forward scattering seems more important in $\text{N}(\text{2D}) + \text{H}_2$ than in $\text{O}(\text{1D}) + \text{H}_2$. For $\text{N}(\text{2D}) + \text{H}_2$, the forward/backward ratio is almost within the statistical limit (as is shown by the excellent agreement with the results of the statistical model which predicts a symmetric DCS) and therefore the small difference in the backward/forward intensity is not really significant.

The QM, SM, and QCT scattering-angle-selected vibrational-state-resolved product translational distributions, $P(E'_T, \Delta\theta)$, for

H_2 initial rotational states $j = 0$ and $j = 1$ are shown in Figures 8 and 9 at $\Delta\theta = 20^\circ$ intervals. The analogous figures for $j = 2$ and $j = 3$ (QCT and SM only) are shown in Supporting Information Figures D and E. In all cases (QM, SM, and QCT), scattering-angle-selected product translational energy distributions, $P(E'_T, \Delta\theta)$, with $\Delta\theta = \theta_2 - \theta_1$, were obtained by using the equation

$$P(E'_T, \Delta\theta) = \sum_k N_k \exp \left[- \left(\frac{E'_T - E_k}{\Delta E_k} \right)^2 \right] \int_{\theta_1}^{\theta_2} \left(\frac{1}{\sigma_R} \frac{d\sigma_R}{d\omega_k} \right) \sin \theta \, d\theta \quad (5)$$

where the sum extends to every rovibrational state $k = (v', j')$ of the NH product, E_k is the H-atom center-of-mass recoil energy corresponding to the NH internal state k , and $(d\sigma_R/d\omega)_k$ is the theoretical (QCT, QM, or SM) v', j' -state-resolved differential cross section. The resolution of the experiment is modeled with a Gaussian function centered at E_k , with normalization constant N_k , and a width of ΔE_k .

The trend already observed for other insertion reactions as $\text{C}(\text{1D}) + \text{H}_2$ ^{34,40} is confirmed in the present case, since the fraction of energy released as products' translational energy E'_T , f_T , is larger in the proximity of the two scattering poles (backward and forward). To illustrate this behavior, some of the f_T values for different angular ranges, $\Delta\theta$, are reported in Table 2. This result clearly indicates that the coupling between

TABLE 2: QM, SM, and QCT Fractions of the Total Available Energy Released as Product Translational Energy, f_T , for the $\text{N}(\text{D}) + \text{H}_2$ Reaction at Selected Angular Ranges, $\Delta\theta$

QM Calculations				
$\Delta\theta$	$j = 0$	$j = 1$	$j = 2$	
0–20°	0.51	0.51	0.49	
80–100°	0.39	0.38	0.37	
160–180°	0.46	0.47	0.43	
QCT Calculations				
$\Delta\theta$	$j = 0$	$j = 1$	$j = 2$	$j = 3$
0–20°	0.53	0.54	0.52	0.48
80–100°	0.35	0.34	0.34	0.32
160–180°	0.50	0.47	0.48	0.41
SM Calculations				
$\Delta\theta$	$j = 0$	$j = 1$	$j = 2$	$j = 3$
0–20° and 160–180°	0.51	0.51	0.51	0.50
80–100°	0.45	0.45	0.45	0.44

the products' angular and translational energy distributions is significant and should be considered in the simulation of the experimental results.

The agreement between the different sets of QM, QCT, and SM $P(E'_T, \Delta\theta)$ is quite good. However, the SM calculations produced a systematically larger fraction of energy associated with the range of θ between 40 and 140°.

IV. Comparison between Experimental Results and Theoretical Predictions

To compare the theoretical results with the measured angular distribution in the most straightforward way, we have transformed the theoretical DCSs derived in the CM frame into the LAB frame, taking into account the averaging over the experimental conditions (beam velocity distributions and angular divergences, detector aperture) and the distribution of initial j 's in the experiment and their relative reactivity. The angle-dependent translational energy distributions, $P(E'_T, \Delta\theta)$, derived in the calculations for each initial j have been used in the simulation. Because of the high sensitivity of the simulation of the LAB distributions to the rise of $P(E'_T, \Delta\theta)$, the angle-dependent translational energy distributions actually used in the simulation are those obtained with a smaller ΔE_k interval (implying a higher resolution) than that used in preparing Figures 8 and 9 (and Supporting Information Figures D and E). It must be noted that the sensitivity of our experimental data is not the same in the whole E'_T range. Thus, the $P(E'_T, \Delta\theta)$ distributions shown in Figures 8 and 9 have been obtained with the average resolution ΔE_k of the experiment.

The resulting LAB angular and TOF distributions are depicted in Figures 10 and 11, respectively, together with the experimental results. As can be appreciated, all theoretical methods are able to reproduce most of the characteristics of the experimental angular distribution. Nevertheless, some differences are visible.

We comment first on the comparison between QM predictions and the experimental results. The LAB angular and TOF distributions obtained by considering the QM angle-dependent $P(E'_T, \Delta\theta)$ compare well with the experimental ones. Essentially, all of the characteristics of the LAB distributions are correctly predicted. However, the comparison is slightly worse with respect to that obtained when simulating the experiment without considering the coupling, that is, by using the global QM $P(E'_T)$ (see Figure 1 of ref 37). The main difference in the LAB angular

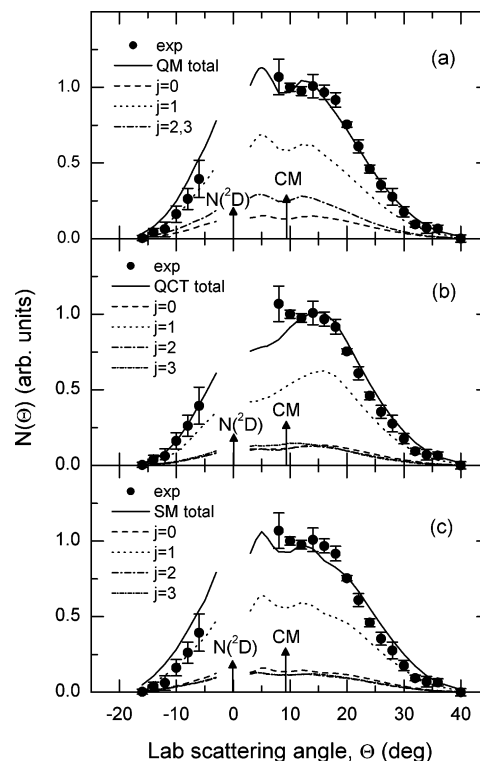


Figure 10. LAB angular distribution as obtained from (a) QM, (b) QCT, and (c) SM CM functions calculated at $E_c = 15.9 \text{ kJ mol}^{-1}$ on the PES by Pederson et al.¹⁴ superimposed to the experimental distribution. The calculated contributions for the separated initial j levels of H_2 are also reported. As can be seen, initial $j = 1$ contributes most to the overall angular distribution.

distribution simulation when considering the angle-dependent $P(E'_T, \Delta\theta)$ is due to the selective coupling of a larger amount of energy released as E'_T for the products scattered around $\theta = 0^\circ$ in the CM frame (see Table 2 and Figures 8 and 9). This has the effect of overestimating the product intensity in the LAB angular range between $\Theta = -16^\circ$ and $\Theta = -6^\circ$. The other features of the LAB angular and TOF distributions are essentially the same as those reported in ref 37 within the experimental uncertainty.

Something similar happens in the QCT simulation of the LAB angular distribution. In this case, however, the larger fraction of energy released as E'_T at the two poles improves the comparison with the experimental results at the LAB negative angles and spoils only slightly the comparison with the intensity at angles larger than 20°.

It might seem surprising that, even though the SM CM DCSs are those which better resemble the best-fit one, the comparison with the LAB distribution is worse than that in the other two cases. The intensity of both wings of the angular distribution is overestimated with respect to the experimental one. An analysis of the characteristics of the SM CM functions indicates that this is due to the systematically larger fraction of energy associated with the SM $P(E'_T, \Delta\theta)$ in the range of θ between 40 and 140° (see Table 2). As already mentioned, the fit of the LAB data is extremely sensitive to the rise of $P(E'_T)$ and also small differences in this respect have a great effect on the shape of the LAB angular distribution.

V. Discussion and Conclusions

As we have seen, the explicit inclusion of the coupling between the product angular and translational energy distributions in the simulation of the experimental results has partly

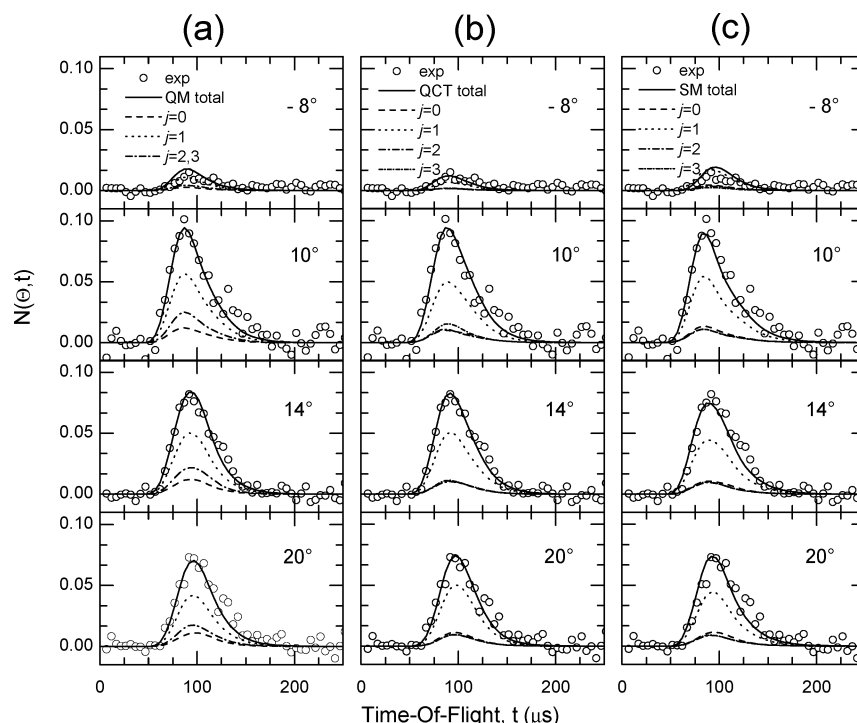


Figure 11. TOF spectra as obtained from (a) QM, (b) QCT, and (c) SM CM functions calculated at $E_c = 15.9 \text{ kJ mol}^{-1}$ on the PES by Pederson et al.¹⁴ superimposed to the experimental distributions. The calculated contributions for the separated initial j of H_2 are also reported.

changed the status of the comparison between the theoretical predictions and experimental results. In any case, the conclusions reached in our previous report on the title reaction³⁷ are still valid.

In particular, the QCT simulation underestimates the experimental angular distribution in the key angular region between $\Theta = 8^\circ$ and $\Theta = 10^\circ$, which corresponds to scattering in the forward hemisphere in the CM frame. This region, in contrast, is well reproduced by the QM simulation within the experimental uncertainty. In this respect, the SM simulation is certainly disappointing, since at the level of the CM DCSs it is the method which better reproduces the best-fit (symmetric) CM angular distribution. However, as already commented on, the reason for such a disagreement in the LAB is completely due to the significantly larger f_T associated with the range of θ around 90° .

To understand the origin of the differences between the classical and quantum predictions, in ref 37, the QM and QCT $(2L + 1)$ degeneracy-weighted reaction probability for the reaction with initial $j = 1$ was reported as a function of the orbital angular momentum, L , and the QM and QCT DCSs were scrutinized as they change with the maximum value of the angular momentum, L_{max} , retained in the partial wave sum. In Figure 12, the QM, SM, and QCT $(2L + 1)$ degeneracy-weighted reaction probabilities are compared for both initial states $j = 0$ and 1. In both cases, the QCT reactivity at $L \geq 12$ is smaller than the QM one, while there is excellent agreement between the QM and SM functions, also in the region of large L (note that $J = L$ for $j = 0$). A more detailed comparison can be done at the level of ν' -state-resolved opacity functions, as seen in Figure 13 for initial $j = 0$ (the situation is in all similar for the other initial j 's, and the relative ν' -state-resolved opacity functions are not shown here). The QM and QCT opacity functions compare well for low and intermediate J values (or, in classical mechanics, with small and intermediate impact parameters) essentially for all ν' states. However, for each ν' state, the QCT reactivity is clearly smaller than QM at the largest

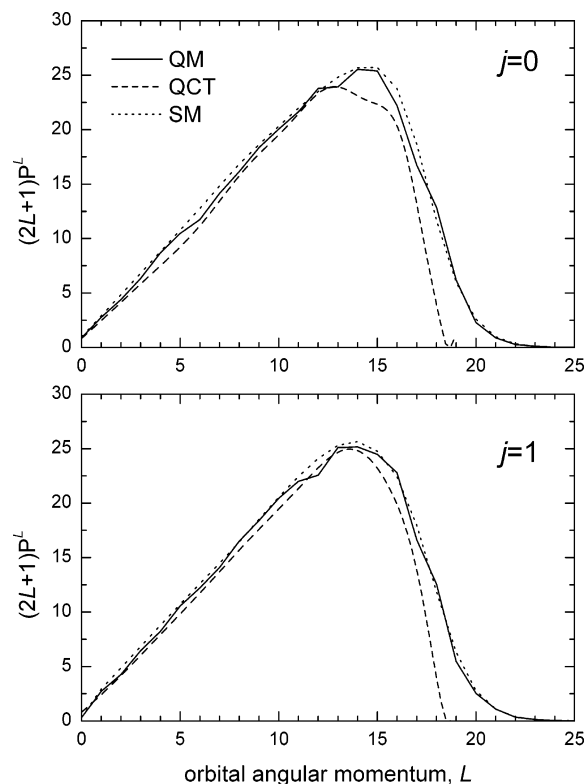


Figure 12. QM, QCT, and SM total $(2L + 1)$ degeneracy-weighted reaction probabilities as a function of the orbital angular momentum, L , for the $\text{N}(^2\text{D}) + \text{H}_2(\nu=0, j=0)$ (top panel) and $\text{N}(^2\text{D}) + \text{H}_2(\nu=0, j=1)$ (bottom panel) reactions calculated on the PES by Pederson et al.¹⁴

angular momenta. In contrast, the comparison between QM and SM is very good at the largest J values for all ν' states, which confirms that the tunneling effects are in all accounted for by the SM method. However, for low and intermediate J values, the SM reactivity is smaller in the case of $\nu' = 0$, quite larger in the case of $\nu' = 2, 3$, and significantly larger for $\nu' = 4$

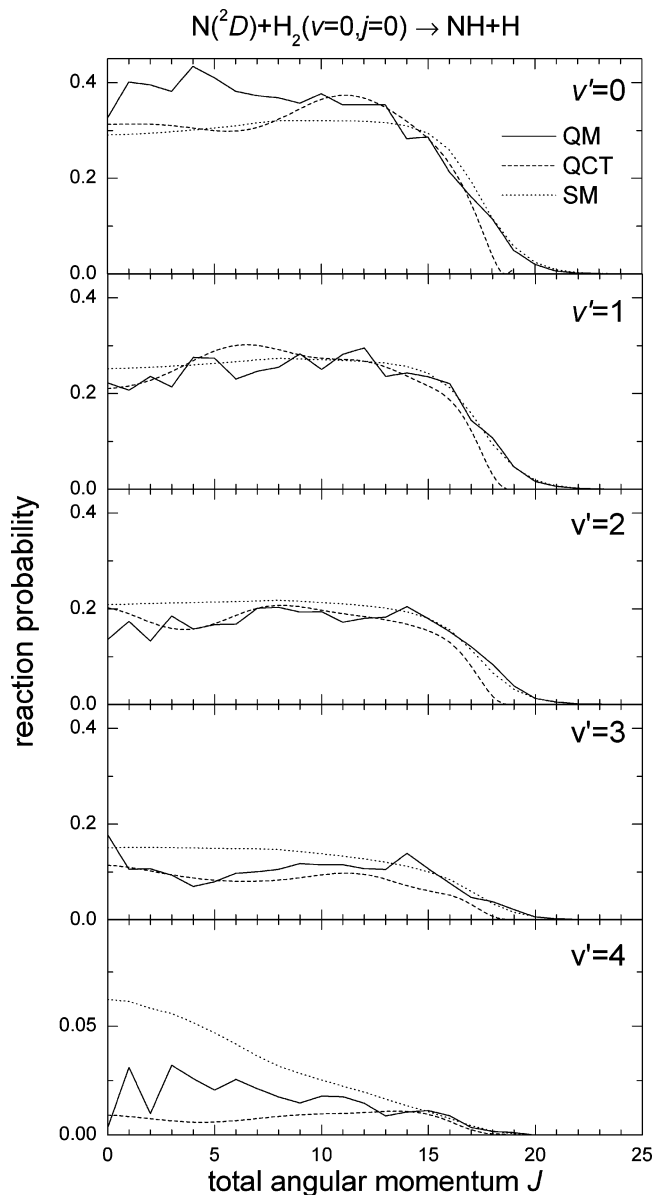


Figure 13. QM, QCT, and SM vibrational-state-resolved reaction probabilities as a function of the total angular momentum, J (here also L), for the $\text{N}(^2\text{D}) + \text{H}_2(v=0, j=0) \rightarrow \text{NH} + \text{H}$ reaction calculated on the PES by Pederson et al.¹⁴

compared to the QM ones. The same trend was observed in the case of initial $j = 1$ (the most populated state in the experiment). It is unclear at the present stage why the QM total reaction probability is so perfectly reproduced by the SM method, while the v' -state-resolved functions are not. As was already pointed out, however, the statistical model works well for sufficiently averaged quantities and “one should be careful not to push it too far”.⁴⁴

In ref 37, the analysis of QM and QCT DCSs as they change with the maximum value of the angular momentum retained in the partial wave sum calculations has brought to the conclusion that the missing forward intensity in the QCT DCS is due to impossibility of the classical approach of considering the tunneling through the centrifugal barriers at the highest total angular momenta that contribute to the reactions. A similar plot is presented here for initial $j = 0$ (top panel of Figure 14) and including the SM functions (bottom panel, Figure 14). Also, in this case, the QM and QCT DCSs, when retained the first partial waves, are essentially coincident, while already at $L_{\text{max}} = 10$ a

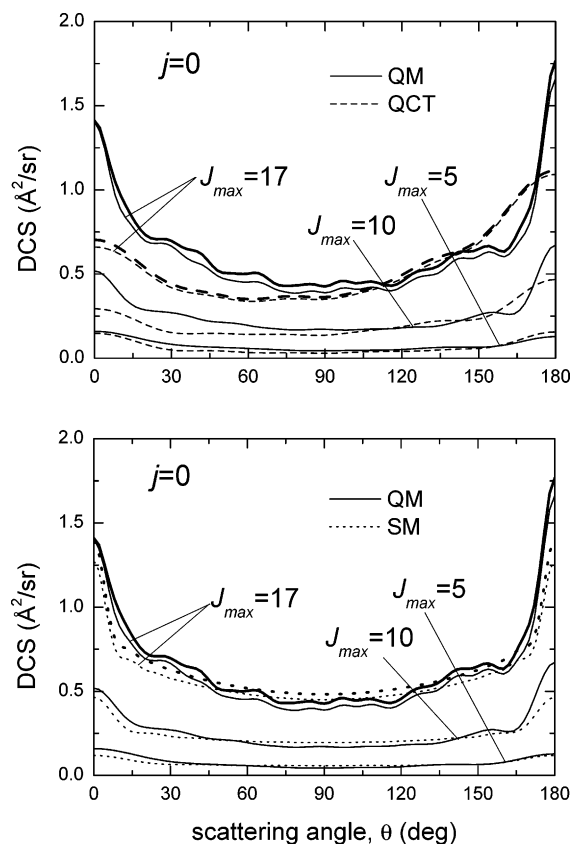


Figure 14. Total differential cross section as a function of the maximum value of the total angular momentum, J_{max} , retained in the partial wave sum for the $\text{N}(^2\text{D}) + \text{H}_2(v=0, j=0)$ reaction calculated on the PES by Pederson et al.¹⁴ Only $J_{\text{max}} = 5, 10$, and 17 values are shown. The thick lines correspond to the converged total differential cross sections ($J_{\text{max}} = 26$). Top panel: comparison between QM and QCT data. Bottom panel: comparison between QM and SM data.

clear difference becomes visible with the QM DCS having a larger intensity in the forward direction. The same comparison with the SM functions reveals an excellent agreement for most of the angular range and values of L_{max} . An important limitation of the SM method, however, is due to the random-phase approximation used to generate the DCSs that can only produce backward/forward symmetric DCS.⁴⁴ Therefore, we cannot expect that the asymmetry of the QM DCSs could be reproduced in any case. However, the SM ratio of sideways-to-forward scattering is in excellent agreement with the QM functions for all values of L_{max} .

In conclusion, the more rigorous simulation of the experimental results by using angle-dependent product translational energy distributions does not change the picture previously obtained for the title reaction. The accuracy of the NH_2 ground state PES of Pederson et al.¹⁴ is substantially confirmed. In this respect, it is interesting to note that the role of the excited state $\text{A}^2\text{A}'$ PES has been recently analyzed. A trajectory-surface-hopping study revealed that the nonadiabatic DCSs, which can account for a maximum contribution of 10% to the overall formation of $\text{NH}(X^3\Sigma^-)$ at collision energies around 20 kJ mol^{-1} , are clearly more backward/forward symmetric than those generated on the ground state PES.⁶⁰ Inclusion of such a contribution can therefore help to improve the comparison with the experimental results. In this regard, future work on this reaction can be envisaged along the lines followed for the similar $\text{O}(^1\text{D}) + \text{H}_2$ reaction.^{24,26,61} In particular, the translational energy dependence of state-resolved differential cross sections may help

to shed light on the possible contribution of the excited state PES, while experiments using *p/o*-H₂ may help to disentangle the effects of reagent rotation.⁶²

Finally, the rigorous statistical model proposed by Manolopoulos and co-workers^{43,44} is confirmed to be a convenient approximate method which can accurately describe some important quantum effects, otherwise missed by the widely used QCT method. Both methods, possibly used jointly, can help in describing the insertion reactions for which the QM calculations are not (yet) feasible.

Acknowledgment. This work was supported by MIUR (COFIN 2003 and FIRB 2001) of Italy and by DGES (BQU2002-04627-C02-02) of Spain. This work was also supported in part by the European Community's Human Potential Programme under contract HPRN-CT-1999-00007 [Reaction Dynamics]. T.G.-L. would like to acknowledge support from the Spanish MEC under grant FIS2004-02461, the program Ramon y Cajal, and the EU Contract No. MERG-CT-2004-513600. The QM hyperspherical coordinate calculations were performed on a NEC-SX5 vector supercomputer, through a grant from the Institut du Développement et des Ressources en Informatique Scientifique (IDRIS) in Orsay, France. It is a pleasure to dedicate to Professor Don Truhlar, on the occasion of his 60th birthday, this paper on a theme—quantum and QCT scattering calculations on accurate potential energy surfaces and comparison with experiment—in which he has been a pioneer and continues to be an inspiration to many of us.

Supporting Information Available: Figures showing QM, QCT, and SM *v'*-state-resolved rotational distributions, differential cross sections, and scattering-angle-selected product translational energy distributions. This material is available free of charge via the Internet at <http://pubs.acs.org>.

References and Notes

- Casavecchia, P.; Balucani, N.; Volpi, G. G. *Annu. Rev. Phys. Chem.* **1999**, *50*, 347.
- Casavecchia, P. *Rep. Prog. Phys.* **2000**, *63*, 355.
- Liu, K. *Annu. Rev. Phys. Chem.* **2001**, *52*, 139.
- Althorpe, S. C.; Clary, D. C. *Annu. Rev. Phys. Chem.* **2003**, *54*, 493.
- Balucani, N.; Skouteris, D.; Cartechini, L.; Capozza, G.; Segoloni, E.; Casavecchia, P.; Alexander, M. H.; Capecchi, G.; Werner, H.-J. *Phys. Rev. Lett.* **2003**, *91*, 013201.
- Skodje, R. T.; Yang, X. *Int. Rev. Phys. Chem.* **2004**, *23*, 253.
- Althorpe, S. C. *Int. Rev. Phys. Chem.* **2004**, *23*, 219.
- Balucani, N.; Skouteris, D.; Capozza, G.; Segoloni, E.; Casavecchia, P.; Alexander, M. H.; Capecchi, G.; Werner, H.-J. *Phys. Chem. Chem. Phys.* **2004**, *6*, 5007.
- Aoiz, F. J.; Bañares, L.; Herrero, V. J. *Int. Rev. Phys. Chem.*, in press.
- Honvault, P.; Launay, J.-M. *J. Chem. Phys.* **1999**, *111*, 6665.
- Honvault, P.; Launay, J.-M. *J. Chem. Phys.* **2001**, *114*, 1057.
- Bañares, L.; Aoiz, F. J.; Honvault, P.; Bussery-Honvault, B.; Launay, J.-M. *J. Chem. Phys.* **2003**, *118*, 565.
- Honvault, P.; Launay, J.-M. *Chem. Phys. Lett.* **2003**, *370*, 371.
- Pederson, L. A.; Schatz, G. C.; Ho, T.-S.; Hollebek, T.; Rabitz, H.; Harding, L. B.; Lendvay, G. R. *J. Chem. Phys.* **1999**, *110*, 9091.
- Pederson, L. A.; Schatz, G. C.; Ho, T.-S.; Hollebek, T.; Rabitz, H.; Harding, L. B. *J. Phys. Chem. A* **2000**, *104*, 2301.
- Ho, T.-S.; Rabitz, H.; Aoiz, F. J.; Bañares, L.; Vázquez, S. A.; Harding, L. B. *J. Chem. Phys.* **2003**, *119*, 3063.
- Dobbyn, A. J.; Knowles, P. J. *Mol. Phys.* **1997**, *91*, 1107.
- Bussery-Honvault, B.; Honvault, P.; Launay, J.-M. *J. Chem. Phys.* **2001**, *115*, 10701.
- Bañares, L.; Aoiz, F. J.; Vázquez, S. A.; Ho, T.-S.; Rabitz, H. *Chem. Phys. Lett.* **2003**, *374*, 243.
- Zyubin, A. S.; Mebel, A. M.; Chao, S. D.; Skodje, R. T. *J. Chem. Phys.* **2001**, *114*, 320.
- Ho, T.-S.; Hollebek, T.; Rabitz, H.; Chao, S. D.; Skodje, R. T.; Zyubin, A. S.; Mebel, A. M. *J. Chem. Phys.* **2002**, *116*, 4124.
- Alagia, M.; Balucani, N.; Cartechini, L.; Casavecchia, P.; Volpi, G. G.; Pederson, L. A.; Schatz, G. C.; Lendvay, G.; Harding, L. B.; Hollebek, T.; Ho, T.-S.; Rabitz, H. *J. Chem. Phys.* **1999**, *110*, 8857.
- Balucani, N.; Alagia, M.; Cartechini, L.; Casavecchia, P.; Volpi, G. G.; Pederson, L. A.; Schatz, G. C. *J. Phys. Chem. A* **2001**, *105*, 2414.
- Liu, X. H.; Wang, C. C.; Harich, S.; Yang, X. *Phys. Rev. Lett.* **2002**, *89*, 133201.
- Liu, X. H.; Lin, J. J.; Harich, S.; Yang, X. *Phys. Rev. Lett.* **2001**, *86*, 408.
- Liu, X. H.; Lin, J. J.; Harich, S.; Schatz, G. C.; Yang, X. *Science* **2000**, *289*, 1536.
- Liu, X. H.; Lin, J. J.; Harich, S.; Yang, X. *J. Chem. Phys.* **2000**, *113*, 1325.
- Hermine, P.; Hsu, Y. T.; Liu, K. *Phys. Chem. Chem. Phys.* **2000**, *2*, 581.
- Hsu, Y. T.; Liu, K.; Pederson, L. A.; Schatz, G. C. *J. Chem. Phys.* **1999**, *111*, 7921.
- Hsu, Y. T.; Liu, K.; Pederson, L. A.; Schatz, G. C. *J. Chem. Phys.* **1999**, *111*, 7931.
- Alagia, M.; Balucani, N.; Cartechini, L.; Casavecchia, P.; van Kleef, E. H.; Volpi, G. G.; Kuntz, P. J.; Sloan, J. J. *J. Chem. Phys.* **1998**, *108*, 6698.
- Balucani, N.; Casavecchia, P.; Aoiz, F. J.; Bañares, L.; Castillo, J. F.; Herrero, V. J. *Mol. Phys.* **2005**, *103*, 1703.
- Bergeat, A.; Cartechini, L.; Balucani, N.; Capozza, G.; Phillips, L.; Casavecchia, P.; Volpi, G. G.; Bonnet, L.; Rayez, J. C. *Chem. Phys. Lett.* **2000**, *327*, 197.
- Balucani, N.; Capozza, G.; Segoloni, E.; Russo, A.; Bobbenkamp, R.; Casavecchia, P.; Gonzalez-Lezana, T.; Rackham, E. J.; Bañares, L.; Aoiz, F. J. *J. Chem. Phys.* **2005**, *122*, 234309.
- Lee, S.-H.; Liu, K. *Appl. Phys.* **2000**, *B71*, 627; *J. Phys. Chem. A* **1998**, *102*, 8637.
- Lee, S.-H.; Liu, K. *Chem. Phys. Lett.* **1998**, *290*, 323.
- Balucani, N.; Cartechini, L.; Capozza, G.; Segoloni, E.; Casavecchia, P.; Volpi, G. G.; Aoiz, F. J.; Bañares, L.; Honvault, P.; Launay, J.-M. *Phys. Rev. Lett.* **2002**, *89*, 013201.
- Aoiz, F. J.; Bañares, L.; Castillo, J. F.; Herrero, V. J.; Martinez-Haya, B.; Honvault, P.; Launay, J.-M.; Liu, X.; Lin, J. J.; Harich, S. A.; Wang, C. C.; Yang, X. *J. Chem. Phys.* **2002**, *116*, 10692.
- Aoiz, F. J.; Bañares, L.; Castillo, J. F.; Brouard, M.; Denzer, W.; Vallance, C.; Honvault, P.; Launay, J.-M. *Phys. Rev. Lett.* **2001**, *86*, 1729.
- Balucani, N.; Capozza, G.; Cartechini, L.; Bergeat, A.; Bobbenkamp, R.; Casavecchia, P.; Aoiz, F. J.; Bañares, L.; Honvault, P.; Bussery-Honvault, B.; Launay, J.-M. *Phys. Chem. Chem. Phys.* **2004**, *6*, 4957.
- Bañares, L.; Aoiz, F. J.; Honvault, P.; Launay, J.-M. *J. Phys. Chem. A* **2004**, *108*, 1616.
- For instance, see for the title reaction: Defazio, P.; Petrongolo, C. *J. Theor. Comput. Chem.* **2003**, *2*, 547.
- Rackham, E. J.; Huarte-Larranaga, F.; Manolopoulos, D. E. *Chem. Phys. Lett.* **2001**, *343*, 356.
- Rackham, E. J.; Gonzalez-Lezana, T.; Manolopoulos, D. E. *J. Chem. Phys.* **2003**, *119*, 12985.
- Lin, S. Y.; Guo, H. *J. Chem. Phys.* **2005**, *122*, 074304; *J. Chem. Phys.* **2004**, *120*, 9907; *J. Phys. Chem. A* **2004**, *108*, 10066.
- Suzuki, T.; Shihira, Y.; Sato, T.; Umamoto, H.; Tsunashima, S. *J. Chem. Soc., Faraday Trans.* **1993**, *89*, 995. Umamoto, H.; Hachiya, N.; Matsunaga, E.; Suda, A.; Kawasaki, M. *Chem. Phys. Lett.* **1998**, *296*, 203.
- The enthalpy of reaction has been derived from the following: Afeefy, H. Y.; Liebman, J. F.; Stein, S. E. *Neutral Thermochemical Data*. In *NIST Chemistry WebBook*; Linstrom, P. J., Mallard, W. G., Eds.; *NIST Standard Reference Database Number 69*; National Institute of Standards and Technology: Gaithersburg, MD (<http://webbook.nist.gov>, accessed June 2005).
- Alagia, M.; Balucani, N.; Casavecchia, P.; Stranges, D.; Volpi, G. G. *J. Chem. Soc., Faraday Trans.* **1995**, *91*, 575.
- Alagia, M.; Aquilanti, V.; Ascenzi, D.; Balucani, N.; Cappelletti, D.; Cartechini, L.; Casavecchia, P.; Pirani, F.; Sanchini, G.; Volpi, G. G. *Isr. J. Chem.* **1997**, *37*, 329.
- Moore, C. E. *Tables of Spectra of Hydrogen, Carbon, Nitrogen, and Oxygen Atoms and Ions*. In *CRC Handbook of Chemistry and Physics*, 76th ed.; Gallagher, J. W., Ed.; CRC Press: Boca Raton, FL.
- Pollard, J. E.; Trevor, D. J.; Lee, Y. T.; Shirley, D. A. *J. Chem. Phys.* **1982**, *77*, 4818.
- Gallagher, R. J.; Fenn, J. B. *J. Chem. Phys.* **1974**, *60*, 3487, 3492.
- Huber, K. P.; Herzberg, G. (data prepared by J. W. Gallagher and R. D. Johnson, III) *Constants of Diatomic Molecules*. In *NIST Chemistry WebBook*; Linstrom, P. J., Mallard, W. G., Eds.; *NIST Standard*

Reference Database Number 69; National Institute of Standards and Technology: Gaithersburg, MD (<http://webbook.nist.gov>, accessed June 2005).

(54) Launay, J.-M.; Le Dourneuf, M. *Chem. Phys. Lett.* **1989**, *163*, 178. Honvault, P.; Launay, J.-M. In *Theory of Chemical Reaction Dynamics*; Lagana, A., Lendvay, G., Eds.; NATO Science Series; 2004; Kluwer Academic Publishers: Dordrecht, The Netherlands, Vol. 145, p 187.

(55) Zare, R. N. *Angular Momentum*; Wiley: New York, 1988.

(56) Aoiz, F. J.; Bañares, L.; Herrero, V. J. *J. Chem. Soc., Faraday Trans.* **1998**, *94*, 2483.

(57) Bonnet, L.; Rayez, J. C. *Chem. Phys. Lett.* **1997**, *277*, 183.

(58) Umemoto, H.; Terada, N.; Tanaka, K. *J. Chem. Phys.* **2000**, *112*, 5762.

(59) Dodd, J. A.; Lipson, S. J.; Flanagan, D. J.; Blumberg, W. A. M.; Person, J. C.; Green, B. D. *J. Chem. Phys.* **1991**, *94*, 4301.

(60) Santoro, F.; Petrongolo, C.; Schatz, G. C. *J. Phys. Chem. A* **2002**, *106*, 8276.

(61) Yang, X. *Int. Rev. Phys. Chem.* **2005**, *24*, 37.

(62) Gray, S. K.; Balint-Kurti, G.; Schatz, G. C.; Lin, J. J.; Liu, X.; Harich, S.; Yang, X. *J. Chem. Phys.* **2000**, *113*, 7330.